Hindawi
Advances in Materials Science and Engineering
Volume 2018, Article ID 5726845, 12 pages
https://doi.org/10.1155/2018/5726845

Research Article

Influences of Process Parameters and Vibration Parameters on the Forming Force in the Ultrasonic-Assisted Incremental Forming Process

Lang Bai, Yan Li, Mingshun Yang, Zimeng Yao, and Zhiyuan Yao

School of Mechanical and Precision Instrument Engineering, Xi'an University of Technology, Xi'an, Shaanxi 710048, China

Correspondence should be addressed to Yan Li; jyxy-ly@xaut.edu.cn

Received 26 July 2018; Accepted 21 October 2018; Published 14 November 2018

Academic Editor: Hongchao Kou

In the field of plastic forming, ultrasonic vibration has the advantages of small forming force and high forming quality, and it has been introduced into a single-point incremental plastic forming technique with high flexibility and high precision. The ultrasonic vibration single-point incremental compound forming technology with all the above advantages has been achieved. To reveal the variation tendency of the forming force under ultrasonic vibration and single-point incremental coupling, the process parameters (layer spacing, tool head radius, and feed rate) and vibration parameters (frequency and amplitude) on the forming force of the composite technology were quantitatively analyzed by theory, simulation, and experiment. The simulation and experimental results showed that ultrasonic vibration can significantly reduce the forming force of the composite technology. Compared with the simulation results, the theoretical results are not only closer to the experimental results but also have a shorter computation time and better prediction effect on the forming force. The change in the process parameters has a linear effect on the forming force, the nonlinearity of the vibratory parameters influences the forming force, and the frequencies and amplitudes in a suitable range allow the forming force to reach a minimum value. These conclusions have some significance for further studies on the ultrasonic vibratory single-point incremental composite forming technology.

1. Introduction

Single-point incremental forming (SPIF), which is a new type of sheet metal-plastic forming technology, solves the problems of the long manufacturing cycle, high cost, and low flexibility associated with traditional sheet metal stamping and has become the subject to scholars' wide attention [1]. However, in the process of SPIF, the existence of sheet springback, sheet bending, tool head deflection, and other factors leads to some defects that affect the surface quality [2], dimensional accuracy [3], and forming limit [4]. The defects are always accompanied by changes in the state of stress. Therefore, the magnitude and direction of the forming force on the contact area between the tool head and the sheet have important influences on the above defects. Therefore, domestic and foreign scholars have put forward some new composite technologies, such as two-point incremental forming [5], electric auxiliary single-point incremental forming [6], and laser-assisted single-point incremental forming [7], in order to avoid defects by changing the magnitude and action mode of the forming force.

The ultrasonic vibratory plastic forming technology is superior to the ordinary plastic forming technology in regard to both difficult-to-form materials and precision forming and is specifically expressed in two aspects: first, it can significantly reduce the yield stress and flow stress; second, it can improve the lubrication effect and change the friction mechanism. The single-point incremental forming process assisted by ultrasonic vibration is taken as the research object. Through theory and experiments, the stress of the sheet in the ultrasonic vibration single-point incremental forming (UV-SPIF) process is analyzed.

The technical principle is shown in Figure 1. The target is a frustum cone with an upward opening. The sheet metal to

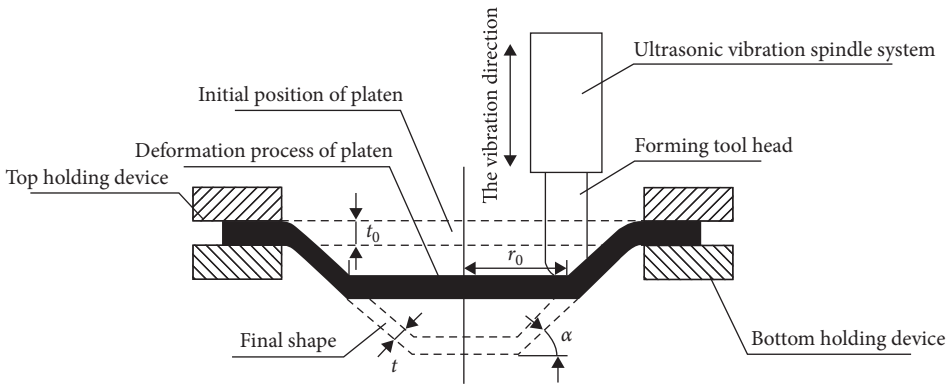

Figure 1: UV-SPIF technology schematic.

be formed is a suitable magnitude metal circular sheet, which is fixed on the workbench with the top and bottom holding devices. The initial position of the sheet is shown with the dashed line above, with an initial thickness of t_0. The tool head forms the sheet metal along the trajectory of the contour line layer by layer. The trajectory is generated discretely in the height direction based on the dimension of the frustum cone. The geometry of the frustum cone determines the magnitude of the forming angle α. The black area in the figure is the current deformation state of the sheet. At this time, the tool head with a radius of r_0 moves in a circular track. The final shape is shown with the lower dashed line in Figure 1.

When the tool head is driven by the ultrasonic vibratory spindle, the sheet can be formed along the trajectory by the tool head with axial ultrasonic vibration. The vibration direction is shown in Figure 1. In this case, the contact state of the tool head and the sheet is not continuous rolling contact under SPIF but high-frequency impact point pressure contact under UV-SPIF. In addition, compared to SPIF, the contact type, stress condition, lubrication state, and plastic flow law of the metal are changed.

Many advantages of ultrasonic vibration in the field of plastic processing are under consideration [8–11], and related scholars have also studied the UV-SPIF technology. Mundo et al. [12] applied high-frequency vibration to a metal sheet for SPIF. It was determined that the vibration improved the surface quality and reduced the distortion of the sheet material. Vahdati et al. [13] demonstrated the effects of the ultrasonic vibration on the reduction of the axial force, springback, and surface roughness of SPIF. Amini et al. [14] applied an axial ultrasonic vibration with a high frequency and low amplitude on the tool head to form a straight flute of 1050 aluminum sheet. It was verified that the ultrasonic vibration could reduce the forming force and improve the formability. Obikawa and Hayashi [15] conducted experiments of UV-SPIF with aluminum alloy, steel, and titanium sheets. It was determined that the ultrasonic vibration could significantly improve the geometric accuracy and forming limit of the parts. Li et al. [16] studied the deformation mechanism of sheets under UV-SPIF via a finite element simulation, obtaining the effect of the amplitude on the magnitude and distribution of the plastic strain.

For studying the variation law of the forming force in the UV-SPIF process, the forming force of SPIF was taken as the starting point of this research. Scholars have conducted significant research in this direction. Henrard [17] established the finite element model and constitutive equation of the forming force in SPIF on the basis of tensile and shear experiments. This approach successfully predicted the force under specific process parameters. Liu [18] explored the influences of the forming force on the forming limit and a sheet thickness of AA7075-O parts. Bagudanch [19] designed special equipment and online control strategies to study the effects of the forming force on the forming angle under different process parameters. Finally, it was confirmed that the forming force increased with an increase in the tool head dimension. Centeno et al. [20] analyzed the influences of the process parameters on the forming properties of the AISI 304 sheet metal via experiments. Additionally, the axial force in the forming process was analyzed. Ankush et al. [21] proposed a predictive model for the forming force in SPIF. The prediction results were compared with the experimental results. As a consequence, the correctness and validity of the predictive model were proven.

Combining the previous research on UV-SPIF by our team [22, 23] with the existing research on the theory of the forming force, an analytical model of the forming force of the UV-SPIF was constructed, and a corresponding simulation model and experimental force measurement platform were built. From the three perspectives of theory, simulation, and experiment, the mapping relationship between the process parameters and the vibration parameters and the forming force is revealed. The variation laws of the forming force under different process parameters and vibration parameters are obtained.

2. Methods

2.1. UV-SPIF Force Analysis. As a common method of analyzing physical problems, the microelement method adopts the concept of a "part to whole." This method can simplify complex physical deformation problems. To explore the force of the sheet in the UV-SPIF technology, the deformation area of the sheet metal was analyzed by means of the microelement method. On this basis, the mechanical

equilibrium equations and the geometric equations were established. In addition, the mapping relationships between the forming force, the forming parameters, and the vibration parameters were calculated.

2.1.1. Mechanical Equilibrium Equations. As the contact area of the tool head on the sheet is hemispherical, the sheet contact area S is close to the spherical shallow pit when the tool head vibrates and impacts the plastic deformation of the sheet, as shown in Figure 2. F_r, F_θ, and F_φ are the vertical, circumferential, and radial forces on the S surface, respectively. v_1 and v_2 are the impact velocity of the tool head in the vibration direction and the feed speed under the control of the numerical control program, respectively. The two velocities through the principle analysis were obtained using the following equations:

$$v_1 = \dot{y} = \frac{\mathrm{d}[A \cdot \sin(2\pi f t)]}{\mathrm{d}t} = 2\pi f A \cdot \cos(2\pi f t),$$
$$v_2 = v, \tag{1}$$

where y is the axial displacement of the tool head; A and f are the amplitude and frequency, respectively, which are constants; and v is the feed speed of the tool head.

In the sheet contact area S, the sheet microelement of the spherical coordinate system was taken as the analysis object, as shown in Figure 3. R is the tool head radius. $\mathrm{d}\theta$ and $\mathrm{d}\varphi$ are the angles of the opposite sides in the height direction of the microelement. σ_r, σ_θ, and σ_φ are the stresses of the microelements in the vertical, circumferential, and radial directions, respectively. In addition, t is the thickness of the microelement sheet. The spherical coordinate stress equilibrium equation was vertically established in the microelement, as shown in the following equation:

$$\begin{aligned}
&\left(\sigma_r + \frac{\partial \sigma_r}{\partial r}\mathrm{d}r\right) \cdot (R+t)^2 \cdot \mathrm{d}\theta \cdot \mathrm{d}\varphi - \sigma_r \cdot (R \cdot \mathrm{d}\theta) \cdot (R \cdot \mathrm{d}\varphi) \\
&+ \sigma_\varphi \cdot \sin\frac{\mathrm{d}\varphi}{2} \cdot \left(\pi \cdot t^2 \cdot \frac{\mathrm{d}\theta}{2\pi} + 2\pi \cdot t \cdot R \cdot \frac{\mathrm{d}\theta}{2\pi}\right) \\
&+ \left(\sigma_\varphi + \frac{\partial \sigma_\varphi}{\partial \varphi}\mathrm{d}\varphi\right) \cdot \sin\frac{\mathrm{d}\varphi}{2} \cdot \left(\pi \cdot t^2 \cdot \frac{\mathrm{d}\theta}{2\pi} + 2\pi \cdot t \cdot R \cdot \frac{\mathrm{d}\theta}{2\pi}\right) \\
&+ \sigma_\theta \cdot \sin\frac{\mathrm{d}\theta}{2} \cdot \left(\pi \cdot t^2 \cdot \frac{\mathrm{d}\varphi}{2\pi} + 2\pi \cdot t \cdot R \cdot \frac{\mathrm{d}\varphi}{2\pi}\right) \\
&+ \left(\sigma_\theta + \frac{\partial \sigma_\theta}{\partial \theta}\mathrm{d}\theta\right) \cdot \sin\frac{\mathrm{d}\theta}{2} \cdot \left(\pi \cdot t^2 \cdot \frac{\mathrm{d}\varphi}{2\pi} + 2\pi \cdot t \cdot R \cdot \frac{\mathrm{d}\varphi}{2\pi}\right) = 0.
\end{aligned} \tag{2}$$

The third-order minute term was eliminated, so the following equation could be obtained:

$$\sigma_r \cdot \mathrm{d}\theta \cdot \mathrm{d}\varphi + \sigma_\varphi \cdot \sin\frac{\mathrm{d}\varphi}{2} \cdot \mathrm{d}\theta + \sigma_\theta \cdot \sin\frac{\mathrm{d}\theta}{2} \cdot \mathrm{d}\varphi = 0. \tag{3}$$

Based on the following two considerations, Equation (3) could be simplified. The first one was that the microelement was arbitrary on the contact surface. Therefore, the triaxial stresses in the contact surface satisfied the relationship of the above formula at every point. The second consideration was that the actual deformation of the sheet in the circumference was far less than the radial stretching and vertical thinning [4]. Therefore, the circumferential strain ε_θ is approximately zero, and the circumferential stress σ_θ is the average stress of the radial stress σ_φ and the vertical stress σ_r. σ_φ and σ_r are opposite to each other, and σ_θ is zero. Therefore, Equation (3) could be simplified to the following equation:

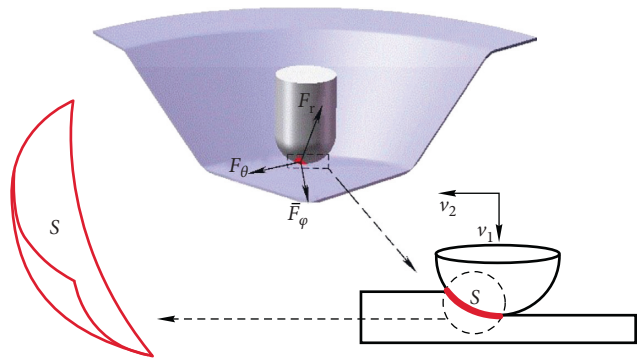

Figure 2: The contact area of the sheet and tool head.

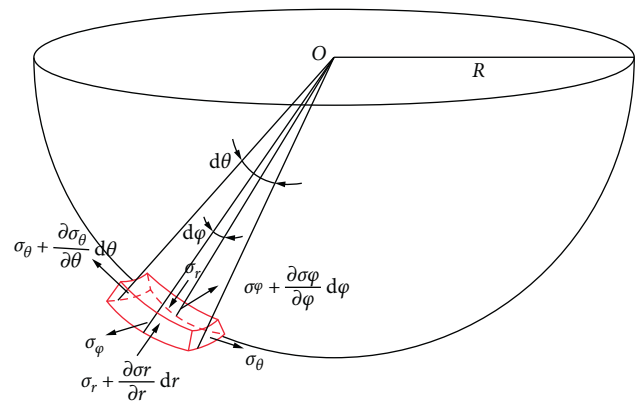

Figure 3: Stress components of the sheet microelement in spherical coordinates.

$$\sigma_r \cdot \varphi + \sigma_\varphi \cdot \sin\frac{\varphi}{2} = 0, \tag{4}$$

where φ is the angle between the front and rear ends of the contact surface S.

According to the yield criterion of the Mises plane deformation, the following relation is known:

$$\sigma_r - \sigma_\varphi = \beta \cdot \sigma_s = \frac{2}{\sqrt{3}}\sigma_s, \tag{5}$$

where σ_s is the yield limit of the sheet.

Equations (4) and (5) were solved simultaneously to obtain the values of σ_φ and σ_r, as shown in the following equations:

$$\begin{cases} \sigma_\varphi = \dfrac{2\sigma_s \cdot \varphi}{\sqrt{3}\,(\varphi + \sin(\varphi/2))}, \\ \sigma_r = \dfrac{4\sigma_s \cdot \varphi + 2\sigma_s \cdot \sin(\varphi/2)}{\sqrt{3}\,(\varphi + \sin(\varphi/2))}, \end{cases} \tag{6}$$

2.1.2. The Geometric Equation of the Contact Region. The geometry and contact area of the tool head are shown in Figure 4. It can be seen that the trajectory of the tool head is a sinusoid in one vibration cycle with a period of T and an amplitude of A. The forming force is P when the amplitude reaches its maximum. P is the combination of the vertical force, the circumferential force, and the radial force, as shown in Equation (7). According to Equation (8), it can be seen that the pressing time of the tool head is very short in one cycle when the vibratory frequency of 20 kHz is taken as an example. Therefore, P can be considered a constant force. Time 1 and time 2 are separated by one vibratory period, and their distance is ΔL. The relationship between the tool feed speed v and the vibratory frequency f is shown in Equation (9):

$$P = \sqrt{F_r^2 + F_\theta^2 + F_\varphi^2}, \tag{7}$$

$$t = \frac{T}{2} = \frac{1}{2f} = \frac{1}{2 \times 20000} = 2.5 \times 10^{-5}\,(\text{unit: s}), \tag{8}$$

$$\Delta L = CE = \frac{v}{f}. \tag{9}$$

According to the geometric relationship of the contact area in Figure 4, the length of OE could be calculated in Equation (10). Then, Equation (11) was derived by the relationship between OE and $\varphi_{\max}$:

$$OE = \sqrt{R^2 + \frac{v^2}{f^2} - \frac{2v}{f}\sqrt{(\Delta z + A) \cdot (2R - \Delta z - A)}}, \tag{10}$$

$$\varphi_{\max} = 2\arccos\frac{OE}{R} = 2\arccos\frac{\sqrt{R^2 + (v^2/f^2) - (2v/f)\sqrt{(\Delta z + A) \cdot (2R - \Delta z - A)}}}{R}. \tag{11}$$

Since the feed rate was in mm/min and the unit of frequency was hertz, the unit of nonuniformity made Equation (11) unable to be calculated. Therefore, it was processed to obtain

$$\varphi_{\max} = 2\arccos\frac{\sqrt{R^2 + (v^2/f^2) \cdot (1/3600) - (v/f) \cdot (1/30)\sqrt{(\Delta z + A) \cdot (2R - \Delta z - A)}}}{R}. \tag{12}$$

2.1.3. Forming Force Analytical Model. Since the constant interval of φ is $[0, \varphi_{\max}]$ and Equation (8) is a function of σ_φ and σ_r with respect to φ, after integration of the independent variables, two radial and vertical forming forces were obtained, as shown in the following equations:

$$F_\varphi = \int_0^{\varphi_{\max}} \frac{2\sigma_s \cdot \varphi}{\sqrt{3}\,(\varphi + \sin(\varphi/2))}\,d\varphi, \tag{13}$$

$$F_r = \int_0^{\varphi_{\max}} \frac{4\sigma_s \cdot \varphi + 2\sigma_s \cdot \sin(\varphi/2)}{\sqrt{3}\,(\varphi + \sin(\varphi/2))}\,d\varphi. \tag{14}$$

2.2. UV-SPIF Force Simulation. Based on the analytical model of the above deformation force, the finite element model of the UV-SPIF process was developed. The model is shown in Figure 5. The effects of the process parameters and vibration parameters on the forming force were explored by the simulation results.

According to the preconditions of the analytical model, the upper and lower platens and the tool head were set as analytically rigid, so they did not deform themselves. In this paper, AL1060 aluminum alloy, which is commonly used in automotive body construction, is selected as the research material, and its yield limit σ_s is 90.2 MPa. Since the thickness of the sheet element was consistent on all sides during the analysis process, it was set as a deformable shell element. The dimension is a square sheet with a side length of 140 mm and an initial thickness of 1 mm. The mesh was divided by an S4R four-node reduced integral shell element with a cell size of 1 mm × 1 mm. The outer radius of the clamp platen is 70 mm, and the inner ring has a radius of 55 mm. Material model selection, contact conditions, boundary conditions, meshing, and other specific settings are shown in Table 1. In addition, the Coulomb friction model was used to describe the friction relationship between the contact pairs. The friction coefficient between the tool head and the sheet was set to 0.1. The coefficients between the sheet and the upper and lower platens were set to 0.2. The translation and rotation of the upper and lower platens in all directions were constrained, and the sheet was clamped by the upper and lower platens.

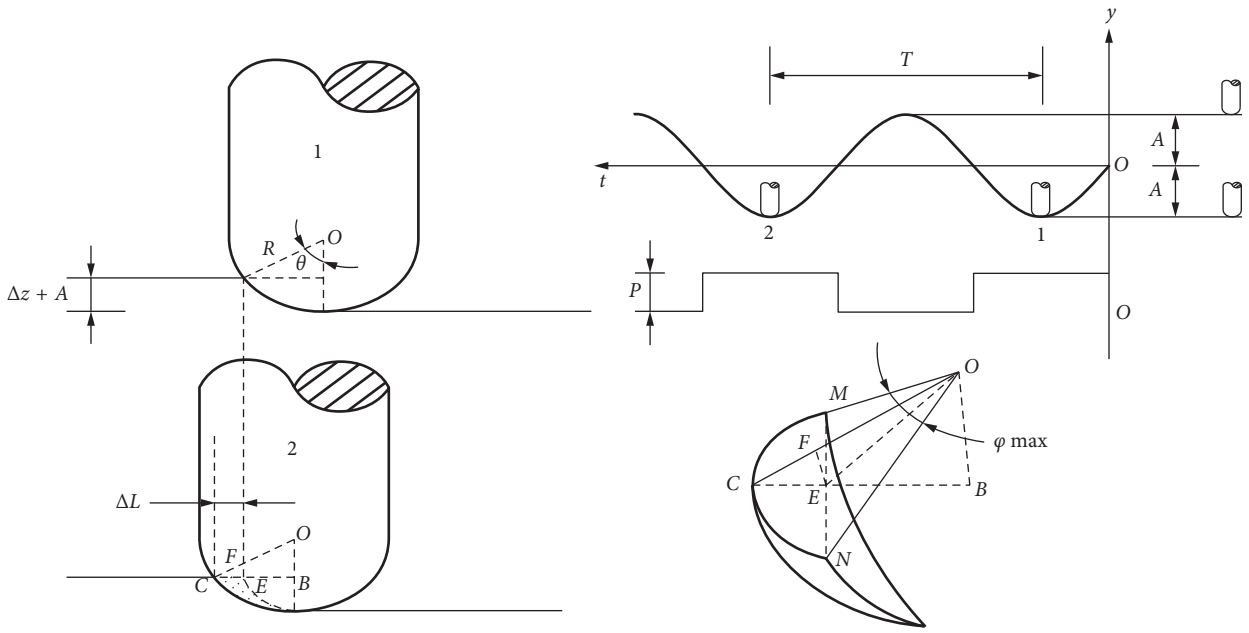

Figure 4: Geometric diagram of the tool head movement.

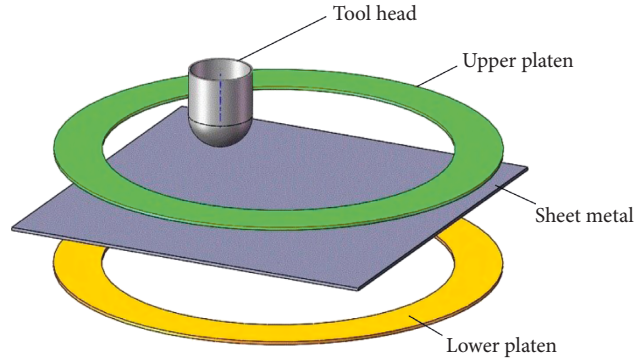

Figure 5: US-SPIF finite element simulation model.

Table 1: Simulation model settings.

Meshing	Workpiece	Grid type: S4R Number of units: 19600
	Tool head	Analytically rigid
Material model selection	Workpiece	Model: plastic model of the shell metal
	Tool head	Material: 1060 aluminum sheet (elastic modulus is 70 GPa; Poisson's ratio is 0.3; density is 2710 kg/m^3)
Contact conditions	Contact type of tool head to sheet: surface-to-surface	
Boundary conditions	Workpiece	6 degrees of freedom on the surface were constrained
	Tool head	Rotation: rotate anticlockwise around the sheet

The amplitude was used as a parameter for the boundary conditions and load constraints. By defining it, it is possible not only to define the movement of the tool head in the horizontal direction but also to apply vertical ultrasonic vibration to the tool head during the UV-SPIF process. The movement of the tool head on each layer is a circular trajectory. This motion can be achieved by a periodic amplitude of the Fourier series. The Fourier series is shown as follows:

$$a = A_0 + \sum_{n=1}^{N} \left[A_n \cos n\omega \left(t - t_0 \right) + B_n \sin n\omega \left(t - t_0 \right) \right], \tag{15}$$

where A_0 is the initial amplitude, N is the number of Fourier series terms, ω is the circular frequency (rad/s), and t_0 is the initial time. Through the Fourier series, the displacement of the tool head in the x and y directions of the horizontal plane

can be realized by the periodic amplitude, as shown in the following equation:

$$x = A\cos 2\pi t, \quad y = A\sin 2\pi t, \tag{16}$$

where A is the radius of each circular layer and t is the forming time of each layer. The trajectories in the x and y directions are combined, that is, the circular trajectory when the tool head forms each layer.

Due to the introduction of ultrasonic vibration, the tool head not only performs a circular motion in the plane but also performs short displacements and high-frequency impact motion in the vertical direction. This motion was constrained by the periodic amplitude so that the displacement of the tool head in the z direction is as follows:

$$z = a\sin[2\pi f(t)], \tag{17}$$

where a is the ultrasonic vibration amplitude and f is the ultrasonic vibration frequency.

2.3. UV-SPIF Force Experiment. UV-SPIF experiments were performed on an Hass high-speed NC milling machine. An ultrasonic vibration spindle and sheet clamping system were designed and developed. A Kistler forming force measurement system was established. Through a large number of experiments, the variation in radial and vertical forces under different processes and vibration conditions was obtained.

2.3.1. UV-SPIF Experiment. The Hass CNC milling machine was used as the UV-SPIF experimental platform, as shown in Figure 6. The upper platen and the lower platen are used to hold the sheet metal. The lower platen is connected with the dynamometer, as shown in Figure 7. Kistler 9257B was used as a force sensor with three directions. The force collected by the sensor was passed to the charge amplifier. Then, the signal was sent to the data acquisition instrument by the charge amplifier. Finally, the force signal was read by the VIBSYS software on the terminal computer.

AL1060 aluminum alloy, which is commonly used in lightweight automobiles, was selected as the experimental material. The material is synthesized by adding a trace amount of copper element to pure aluminum. Therefore, the material has excellent plastic forming properties, good electrical conductivity, better welding property, and strong corrosion resistance [24]. The main chemical composition of the AL1060 aluminum alloy is shown in Table 2. The tool head was grounded from a tungsten steel rod. It has high hardness, rigidity, and wear resistance to ensure that it is not easily deformed during the forming process. A sheet metal was formed by the tool head along a predetermined trajectory under the command of a numerical control program.

To quantitatively study the influence of the frequency and amplitude on the forming force, a stepless frequency modulation ultrasonic generator was selected as the vibration generator. The vibratory frequency of the generator is continuously adjustable from 13 kHz to 75 kHz, and the adjustment is accurate to 0.1 kHz. The generator was

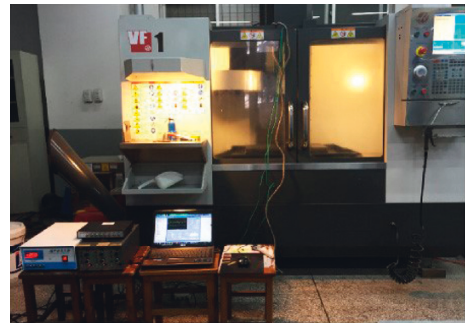

Figure 6: Hass CNC milling machine.

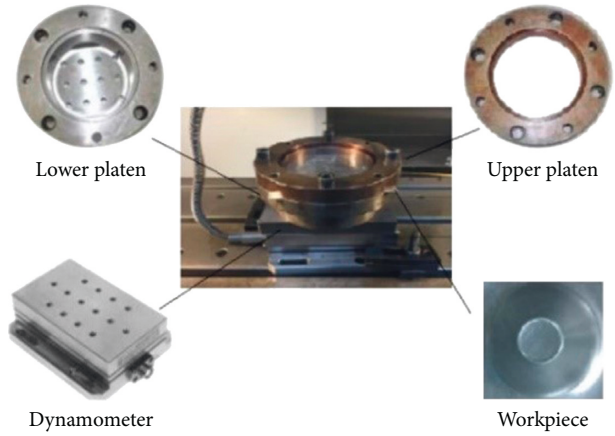

Figure 7: Sheet holding system.

Table 2: The main chemical composition of the AL1060 aluminum alloy (%, mass fraction).

Chemical element	Al	Cu	Ti	Zn	Si	Mg	Mn	Fe
Content (%)	99.63	0.03	0.02	0.03	0.12	0.02	0.01	0.14

connected to the vibration spindle system via a conductor. The spindle system was composed of a transducer, amplitude transformer, and spindle shell. The transducer and amplitude transformer were mounted inside the spindle shell as internal components. One end of the vibratory spindle was connected to the machine tool holder, and the other end was connected to the tool head. The connection between the vibratory spindle and the tool holder was realized through a coupling, which is a stepped sleeve. The upper small circle and the tool holder were connected coaxially through the connecting thread. The lower large circle was connected through fixing screws and locknuts to ensure the coaxiality of the connection between the tool holder and the vibratory spindle in four directions, as shown in Figure 8. The vibratory spindle and the tool head were connected by a fine thread with an outer diameter of 10 mm and a pitch of 1 mm. Since the forming process was accompanied by a certain vibration, a locknut was also installed between the tool head and the spindle. After assembling the vibratory system and the force-measuring system, a corresponding numerical control program was established according to the shape and magnitude of the target. The UV-SPIF experiments were

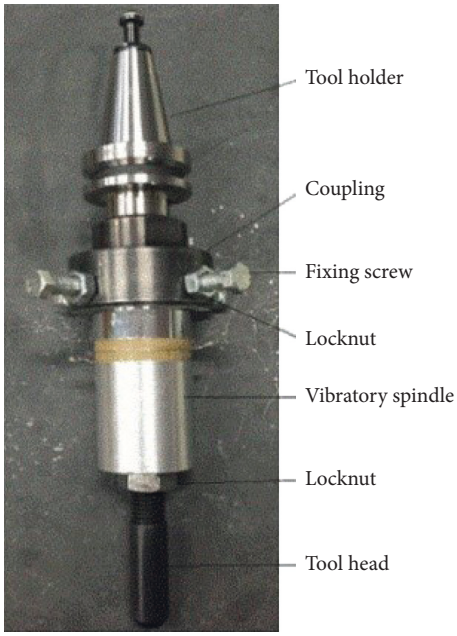

Figure 8: Vibratory spindle system.

performed on the AL1060 aluminum alloy sheet. The experimental process is shown in Figure 9.

3. Results and Discussion

3.1. Volume and Surface Effects of Ultrasonic Vibration. Based on the SPIF simulation process, an ultrasonic vibration (f = 20 kHz and A = 0.02 mm) was applied to the tool head to obtain a UV-SPIF stress nephogram, as shown in Figure 10(b). The SPIF and UV-SPIF experiments were performed under the same process parameters. The SPIF and UV-SPIF parts were obtained, as shown in Figure 11. According to the simulated numerical values of the nephogram and experimental components, it can be seen that the surface quality of the workpiece was improved by the ultrasonic vibration. At the same time, the forming stress was effectively reduced. This result confirms the volume effect and surface effect of ultrasonic vibration on the sheet metal forming process.

The experimental results of UV-SPIF (f = 20 kHz and A = 0.02 mm) and SPIF were compared and analyzed (the forming force was the axial force F_z, which was taken as the analysis object), as shown in Figure 12. A frustum cone was used as the target component, with a total of 20 layers being formed. The average axial force of each layer was taken to generate its law curve about the number of forming layers. It can be seen that the axial force of UV-SPIF and SPIF increased with an increase in the number of layers and reached stability on the 10th lap. It can also be seen that the ultrasonic vibration did not affect the variation law of the axial force with respect to the number of layers. After the analysis and calculation, the axial force of UV-SPIF was reduced by 23.61% compared with that of SPIF.

3.2. Analysis of Theoretical, Simulation, and Experimental Results. The analytical modeling coordinate system was based on a deformation ramp S. The different direction from the direction of the coordinate system was established by the experiment and simulation, which was based on the initial sheet plane. Therefore, the three results could not be compared directly. It was necessary to uniformly process the directions of the forming force in advance.

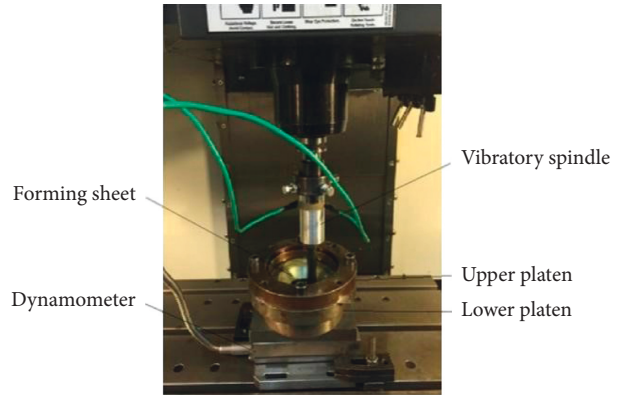

Figure 9: Forming process.

3.2.1. Processing the Coordinate System Directions. The original sheet plane was used as the x-y plane and the perpendicular direction as the z-axis in the experimental and simulated coordinate systems. However, the analytical modeling coordinate system was based on the spatial geometry of the contact area between the tool head and the sheet, as shown in Figure 2. Although there were differences in the directions of the two coordinates, there was a certain relationship in terms of geometric relations, as shown in Figure 13.

When the tool head forms the sheet via UV-SPIF technology with the feed rate F, the forces in the analytical modeling coordinate system are as follows: radial force F_φ, circumferential force F_θ, and vertical force F_r. The forces in the experimental force measurement coordinate system are as follows: F_x, F_y, and F_z. The microelement on the contact area S of the sheet with the tool head (Figure 2) was used as the analysis target (the left side of Figure 13). In the analytical modeling process, the sheet material was considered to be only affected by the radial force F_φ in the x-y plane. In addition, F_φ is the resultant force of F_x and F_y, as shown in Equation (18). The tool head was used as the study object (the right side of Figure 13). The OH is perpendicular to the CD, and the foot point is H. Equation (19) can be obtained from the geometry of the tool head. Therefore, the relationship between the vertical force F_r and the axial force F_z could be calculated by Equation (20). In addition, the analytical model was an ideal model, which did not consider friction. Therefore, the friction F_t downward from the contact area S was not considered.

$$F_\varphi = \sqrt{F_x^2 + F_y^2}, \tag{18}$$

$$\frac{F_r}{F_z} = \frac{OH}{OD} = \frac{CB}{CD} = \sqrt{1 - \frac{\Delta z + A}{2R}}, \tag{19}$$

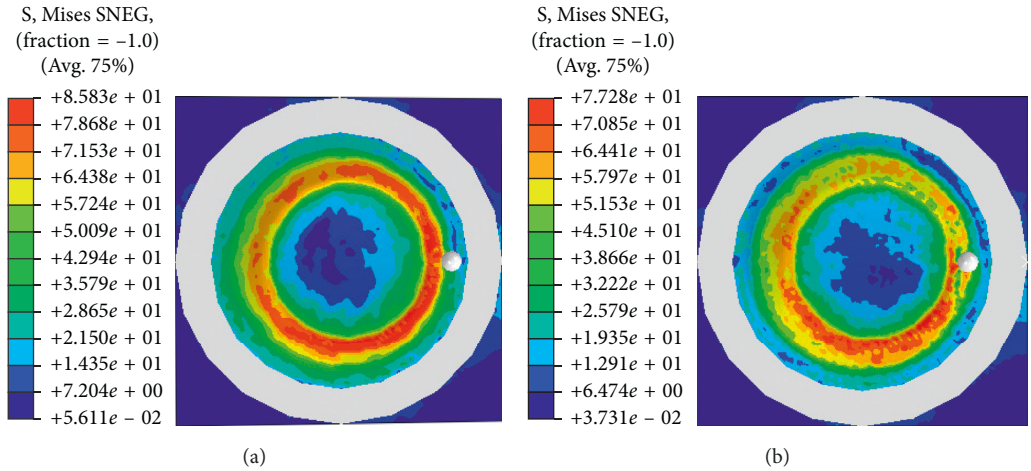

Figure 10: Nephogram of SPIF (a) and UV-SPIF (b).

Figure 11: Workpieces of SPIF (a) and UV-SPIF (b).

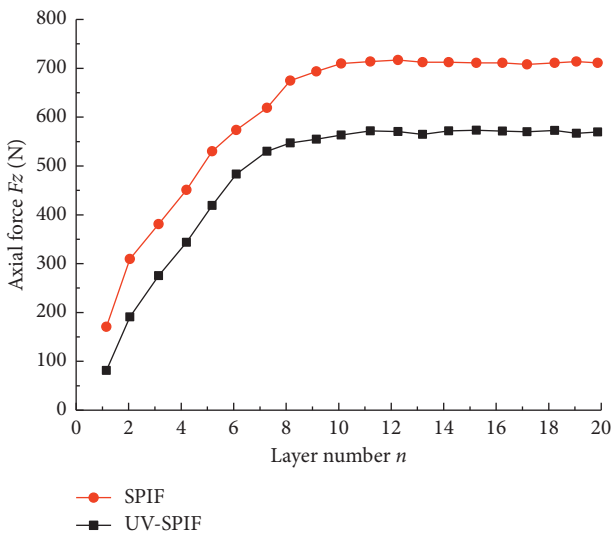

Figure 12: Comparison of axial force in SPIF and UV-SPIF

$$F_r = F_z \cdot \sqrt{1 - \frac{\Delta z + A}{2R}}, \tag{20}$$

3.2.2. Comparative Analysis of the Three Results. Adopting theory, simulation, and experiment as analysis methods, the relationships between the process parameters, vibration parameters, and forming force were studied using the control variable method. As shown in Figures 14–18, the influences of the amplitude, frequency, radius of the tool head, layer spacing, and feed speed on the forming force are shown in order. It can be seen that the theoretical and simulation results followed the experimental results, and their performance trends were consistent. Among the results, simulation F_r < theory F_r < experiment F_r, so it could be considered that the prediction ability of the analytical model was stronger than the simulation results. Due to the partial idealization of the two models, the resulting values of the theory and simulation were lower than the experimental

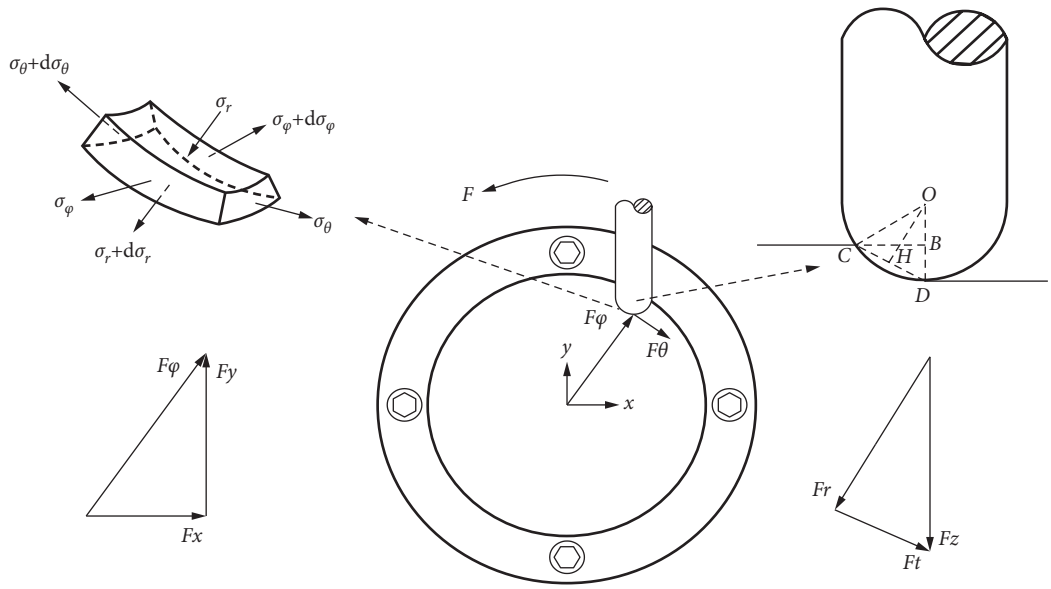

Figure 13: Relationship of the forming forces in different coordinate systems.

values. The theoretical F_φ and simulation F_φ values were also lower than the experimental F_φ values for the same reason as mentioned above. The circumferential force was ignored during the derivation of the theoretical analytical model; therefore, the theoretical F_φ value was smaller than the simulation F_φ value.

In Figure 14, $f = 20$ kHz, $\Delta z = 1.0$ mm, $R = 5$ mm, and $v = 100$ mm/min were constant, and the amplitude was variable. The variation laws of the forming forces with respect to amplitude were obtained in theory, simulation, and experiment. F_r is nonlinearly related to A, and F_φ is linearly related to A. When $A < 0.03$ mm, the sheet was not sufficient to be fully yielded by the tool head. When the tool head was separated from the sheet, the elastic energy was released. The instantaneous springback maintained the contact between the tool head and the sheet, making F_r increase. When A was 0.03 mm, the instantaneous impact force of the tool head exceeded the yield limit of 1060AL. Therefore, the springback was suppressed, and the moment of separation F_r was zero. When $A > 0.03$ mm, the press distance of the tool head was increased to within a vibration cycle. The deformation energy increased with the deformation of the material, which led to F_r increase. As the amplitude increased, the radial deformation increased and F_φ also increased.

In Figure 15, $A = 0.01$ mm, $\Delta z = 1.0$ mm, $R = 5$ mm, and $v = 100$ mm/min were constant, and the frequency varied. The variation laws of the forming forces with respect to frequency were obtained in the three aspects of theory, simulation, and experiment. F_r is nonlinearly related to f, and F_φ is linearly related to f. When $f < 30$ kHz, the hit rate of the tool head increased with an increase in f. The activity of the sheet material was increased due to the vibration of the particles in the interior sheet. The sheet temperature increased, which led to softening of the material. Plastic reinforcement made the sheet easily deform, and it made F_r decrease. When $f > 30$ kHz, excessive frequency increased the instantaneous deformation of the sheet, making the corresponding F_r increase. The increase in frequency led to a reduction in the radial deformation. Therefore, F_φ decreased.

In Figure 16, $A = 0.01$ mm, $f = 20$ kHz, $\Delta z = 1.0$ mm, and $v = 100$ mm/min were constant, and the tool head radius was variable. The variation laws of the forming forces about the radius of the tool head were obtained in terms of theory, simulation, and experiment. Both F_r and F_φ are linearly related to R because an increase in the radius of the tool head directly affects the deformation of the sheet material. However, when R was too small, a stress concentration tended to occur, so the parts were prone to cracks. When R was too large, it was not conducive to forming complex parts. Therefore, the different magnitudes of the tool heads should be selected for parts with different complexity. Within the scope of satisfying the forming ability, the tool head with a larger radius should be selected.

In Figure 17, $A = 0.01$ mm, $f = 20$ kHz, $R = 5$ mm, and $v = 100$ mm/min were constant, and the layer spacing in the forming process was variable. The variation laws of the forming force about the layer spacing were obtained in theory, simulation, and experiment. Both F_r and F_φ are linearly related to Δz. The degree of correlation is greater than the effect of R on the force, which is because a greater sheet deformation was caused by an increase in Δz. However, if Δz was too small, the forming efficiency was low. When Δz was too large, the sheet was prone to bending and springback. Therefore, Δz should be increased under the requirements of satisfying the accuracy. Δz should also be reduced under the formation of complex features.

In Figure 18, $A = 0.01$ mm, $f = 20$ kHz, $R = 5$ mm, and $\Delta z = 1.0$ mm were constant, and the feed speed of tool head forming was variable. The variation laws of the forming force with respect to the feed speed were obtained in the three aspects of theory, simulation, and experiment. Both F_r and F_φ are linearly related to v. The slope of the curve is the lowest.

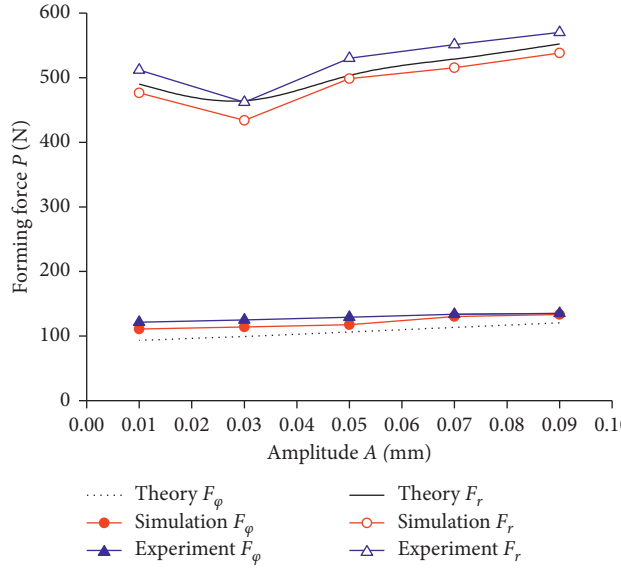

Figure 14: Effect of amplitude on the forming force.

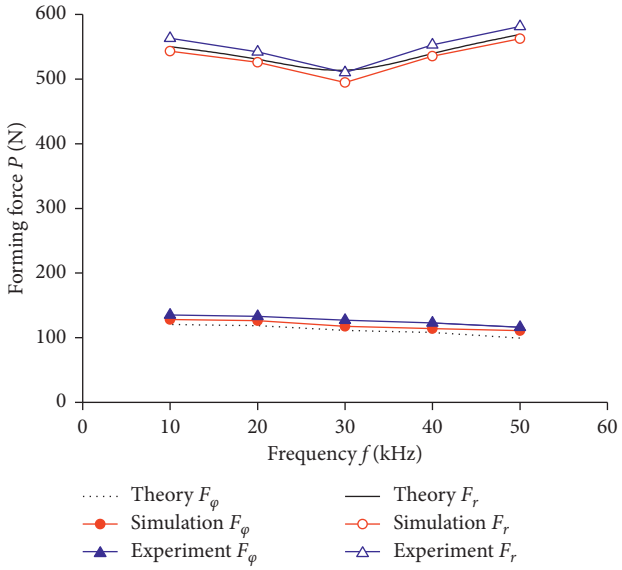

Figure 15: Effect of frequency on the forming force.

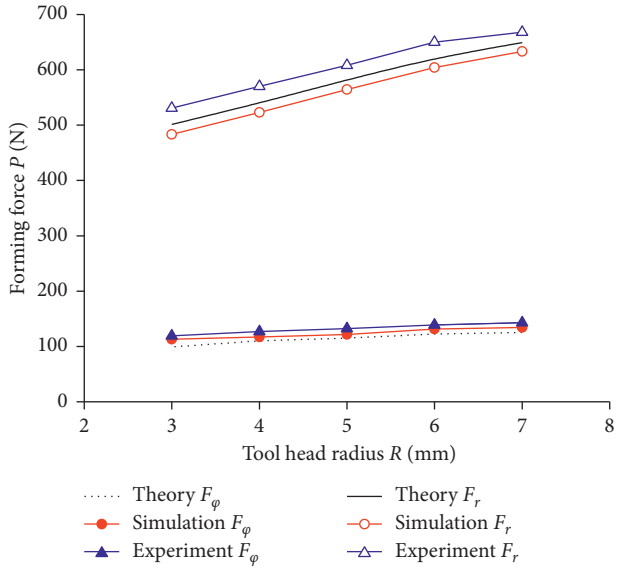

Figure 16: Effect of the tool head radius on the forming force.

Because the instantaneous deformation time of the sheet was only 2.5×10^{-5} seconds, the change in the feed speed had minimal effect on the instantaneous deformation of the sheet. For improving the forming efficiency, v should be increased as much as possible. However, when v was too large, the metal in the interior sheet could not be recovered or recrystallized in time. At this time, the plasticity would become lower, and stress concentrates and cracks could occur.

4. Conclusion

The forming principle and movement rule of the UV-SPIF technology were analyzed. The stress conditions at the sheet deformation area were clarified and interpreted analytically. Furthermore, a mathematical analytical model adapting to the UV-SPIF technology was deduced. A corresponding simulation model was established to simulate the force of the sheet in the UV-SPIF process. The experimental platform and force measurement system were set up to study the influences of various process parameters and vibration parameters on the forming force of UV-SPIF. By comparing and analyzing the results of the three aspects, the following conclusions are drawn:

(1) The axial force on the sheet material is reduced by 23.61% after the axial ultrasonic vibration ($f = 20$ kHz and $A = 0.02$ mm), confirming the volume effect of the ultrasonic vibration in metal-plastic forming. In addition, the changes in the forming force cause the macroscopic springback and the microscopic lattice of

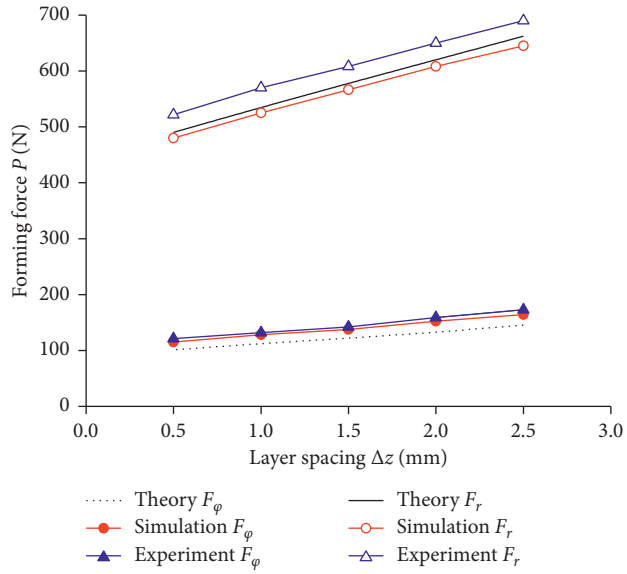

Figure 17: Effect of layer spacing on the forming force.

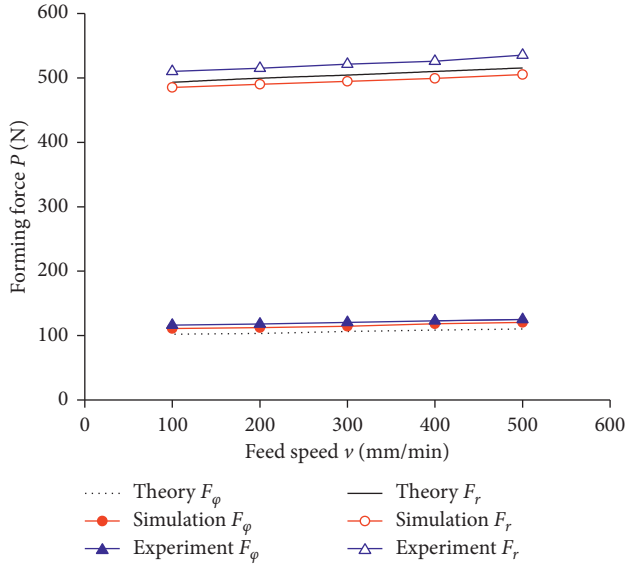

Figure 18: Effect of feed speed on the forming force.

the sheet to change accordingly, which has a certain influence on the surface quality, dimensional accuracy, and forming limit of the final piece.

(2) It is determined that the influence of A and f on F_φ is linear, and the influences on F_r are nonlinear. A and f can reduce the forming force by changing the deformation energy and microstructure of the sheet, and this changing relationship is nonlinear. Therefore, there is a range of frequencies and amplitudes that can minimize the forming force.

(3) When the vibration parameters are constant, the influences of R, Δz, and F on F_φ and F_r are linear. Compared with previous studies [25], the ultrasonic vibration has minimal interference with the mapping relationship between the process parameters and the forming forces. Therefore, previous research conclusions about the effects of the process parameters on the forming force can be applied to the study of UV-SPIF.

Data Availability

The .xlsx data and .mov data used to support the findings of this study have been uploaded to the public database Figshare (DOI: 10.6084/m9.figshare.6953402; https://figshare.com/s/599b84c0f6b5dba904af). Other data used to support the study are included in the article, such as material data, simulation model data, and experimental platform data. These data have no restrictions and are accessible to other researchers.

Conflicts of Interest

The authors declare that they have no conflicts of interest.

Acknowledgments

The authors would like to acknowledge the National Natural Science Foundation of China (51475366 and 51475146), the Science and Technology Planning Project of Shaanxi Province (Grant No. 2016JM5074), and the Key Laboratory of Scientific Research Projects of Shaan'xi Educational Committee (Grant No. 12JS072).

References

[1] A. K. Behera, R. A. de Sousa, G. Ingarao, and V. Oleksik, "Single point incremental forming: an assessment of the progress and technology trends from 2005 to 2015," *Journal of Manufacturing Processes*, vol. 27, pp. 37–62, 2017.

[2] S. Kurra, N. H. Rahman, S. P. Regalla, and A. K. Gupta, "Modeling and optimization of surface roughness in single point incremental forming process," *Journal of Materials Research and Technology*, vol. 4, no. 3, pp. 304–313, 2015.

[3] Y. Li, H. Lu, W. J. T. Daniel, and P. A. Meehan, "Investigation and optimization of deformation energy and geometric accuracy in the incremental sheet forming process using response surface methodology," *International Journal of Advanced Manufacturing Technology*, vol. 79, no. 9–12, pp. 2041–2055, 2015.

[4] C. Raju, N. Haloi, and C. Sathiya Narayanan, "Strain distribution and failure mode in single point incremental," *Journal of Manufacturing Processes*, vol. 30, pp. 328–335, 2017.

[5] M. A. Davarpanah, Z. Zhang, S. Bansal, J. Cao, and R. Malhotra, "Preliminary investigations on double sided incremental forming of thermoplastics," *Manufacturing Letters*, vol. 8, pp. 21–26, 2016.

[6] R. Liu, B. Lu, D. Xu et al., "Development of novel tools for electricity-assisted incremental sheet forming of titanium alloy," *The International Journal of Advanced Manufacturing Technology*, vol. 85, no. 5–8, pp. 1137–1144, 2016.

[7] A. Mohammadi, H. Vanhove, A. Van Bael, and J. R. Duflou, "Towards accuracy improvement in single point incremental forming of shallow parts formed under laser assisted conditions," *International Journal of Material Forming*, vol. 9, no. 3, pp. 339–351, 2016.

[8] Z. Xie, Y. Guan, J. Zhai, L. Zhu, and C. Zhong, "Study on ultrasonic vibration assisted upsetting of 6063 aluminum alloy," *Procedia Engineering*, vol. 207, pp. 490–495, 2017.

[9] S. A. Sajjady, H. Nouri Hossein Abadi, S. Amini, and R. Nosouhi, "Analytical and experimental study of topography of surface texture in ultrasonic vibration assisted turning," *Materials and Design*, vol. 93, pp. 311–323, 2016.

[10] M. M. Molaie, J. Akbari, and M. R. Movahhedy, "Ultrasonic assisted grinding process with minimum quantity lubrication using oil-based nanofluids," *Journal of Cleaner Production*, vol. 129, pp. 212–222, 2016.

[11] B. Yang and M. Yang, "The influence of superimposed ultrasonic vibration on surface asperities deformation," *Journal of Materials Processing Technology*, vol. 229, pp. 367–374, 2016.

[12] D. Mundo, G. Gatti, G. Ambrogio et al., "Considerations on process performance in incremental forming by inducing high frequency vibration," in *Proceedings of EUCOMES 08*, pp. 523–530, Dordrecht Netherlands, January 2009.

[13] M. Vahdati, R. Mahdavinejad, and S. Amini, "Investigation of the ultrasonic vibration effect in incremental sheet metal forming process," *Proceedings of the Institution of Mechanical Engineers, Part B: Journal of Engineering Manufacture*, vol. 231, no. 6, pp. 971–982, 2015.

[14] S. Amini, A. H. Gollo, and H. Paktinat, "An investigation of conventional and ultrasonic-assisted incremental forming of annealed AA1050 sheet," *International Journal of Advanced Manufacturing Technology*, vol. 90, no. 5, pp. 1569–1578, 2017.

[15] T. Obikawa and M. Hayashi, "Ultrasonic-assisted incremental microforming of thin shell pyramids of metallic foil," *Micromachines*, vol. 8, no. 5, p. 142, 2017.

[16] Y. Li, X. Chen, J. Sun, J. Li, and G. Zhao, "Effects of ultrasonic vibration on deformation mechanism of incremental point-forming process," *Procedia Engineering*, vol. 207, pp. 777–782, 2017.

[17] C. Henrard, C. Bouffioux, P. Eyckens et al., "Forming forces in single point incremental forming: prediction by finite element simulations, validation and sensitivity," *Computational Mechanics*, vol. 47, no. 5, pp. 573–590, 2010.

[18] Z. Liu, Y. Li, and P. A. Meehan, "Experimental investigation of mechanical properties, formability and force measurement for AA7075-O aluminum alloy sheets formed by incremental forming," *International Journal of Precision Engineering and Manufacturing*, vol. 14, no. 11, pp. 1891–1899, 2013.

[19] I. Bagudanch, G. Centeno, C. Vallellano, and M. L. Garcia-Romeu, "Forming force in single point incremental forming under different bending conditions," *Procedia Engineering*, vol. 63, pp. 354–360, 2013.

[20] G. Centeno, I. Bagudanch, A. J. Martínez-Donaire, M. L. García-Romeu, and C. Vallellano, "Critical analysis of necking and fracture limit strains and forming forces in single-point incremental forming," *Materials and Design*, vol. 63, pp. 20–29, 2014.

[21] A. Bansal, R. Lingam, S. K. Yadav, and N. Venkata Reddy, "Prediction of forming forces in single point incremental forming," *Journal of Manufacturing Processes*, vol. 28, pp. 486–493, 2017.

[22] P. Li, J. He, Q. Liu et al., "Evaluation of forming forces in ultrasonic incremental sheet metal forming," *Aerospace Science and Technology*, vol. 63, pp. 132–139, 2017.

[23] Y. Li, L. Bai, M. Yang et al., "Research on forming force in single point incremental forming with ultrasonic vibration," *Mechanical Science and Technology for Aerospace Engineering*, vol. 37, no. 2, pp. 270–275, 2018.

[24] Z. J. Wang, M. Ma, Z. X. Qiu et al., "Microstructure, texture and mechanical properties of AA 1060 aluminum alloy processed by cryogenic accumulative roll bonding," *Materials Characterization*, vol. 139, pp. 269–278, 2018.

[25] H. Xu, P. Yi, W. An et al., "Simulation and experimental study of sheet metal single point incremental forming force," *Chinese Journal of Applied Mechanics*, vol. 32, no. 6, pp. 1062–1068, 2015.